Bi-material nanofibrous electrospun junctions: A versatile tool to mimic the muscle–tendon interface

Alberto Sensini [a,b,*], Riccardo D'Anniballe [c], Carlo Gotti [d], Gregorio Marchiori [e], Gianluca Giavaresi [e], Raffaella Carloni [c], Maria Letizia Focarete [f,g], Andrea Zucchelli [a,d,*]

[a] Department of Industrial Engineering, Alma Mater Studiorum - Università di Bologna, Bologna, Italy
[b] CTR and cBITE Departments, MERLN Institute for Technology-Inspired Regenerative Medicine, Maastricht University, Maastricht, the Netherlands
[c] Bernoulli Institute for Mathematics, Computer Science and Artificial Intelligence, Faculty of Science and Engineering, University of Groningen, Groningen, the Netherlands
[d] Advanced Mechanics and Materials, Interdepartmental Center for Industrial Research (CIRI-MAM), Alma Mater Studiorum, Università di Bologna, Bologna, Italy
[e] Surgical Sciences and Technologies, IRCCS Istituto Ortopedico Rizzoli, Bologna, Italy
[f] Department of Chemistry' G. Ciamician' and INSTM UdR of Bologna, Alma Mater Studiorum, Università di Bologna, Bologna, Italy
[g] Health Sciences and Technologies - Interdepartmental Center for Industrial Research (CIRI-HST), Alma Mater Studiorum-Università di Bologna, Bologna, Italy

ARTICLE INFO

ABSTRACT

Soft robotics aims to replicate the structure and mechanics of skeletal muscles. The challenge lies in seamlessly integrating these muscle-inspired soft actuators with the joints they intend to actuate, resembling the natural connection between muscles and tendons (i.e., myotendinous junction). This study addresses this issue by producing electrospun bundles of aligned nanofibers using a thermoplastic polyurethane, mimicking the muscle fascicle, and nylon 6.6 for the tendon one. A novel method was developed to create electrospun bi-material bundles with two different types of myotendinous-inspired junctions, called flat and conical. Scanning electron microscopy and microtomography analyses confirmed that conical junctions mimicked natural myotendinous structures better than flat ones. Tensile mechanical tests demonstrated that bi-material junctions reached stress at failure comparable to polyurethane bundles (11 ± 2 MPa), with the conical junction showing stiffness (0.13 ± 0.02 N/mm) and net elastic modulus (153 ± 10 MPa) values closer to the natural myotendinous ones. Cyclic tests verified the mechanical stability of junctions and their ability to dampen nylon 6.6 hardening over time. Moreover, all bundles withstood cyclic loading without breaking. These findings suggest the potential of biomimetic electrospun junctions for applications in soft robotics, marking a significant step toward advancing this field.

1. Introduction

In recent years, soft robotics has received increasing attention due to its primary focus on designing biomimetic actuators capable of generating movements and replicating natural muscles' elasticity and tunable stiffness [1,2]. These structures enable a better adaptation and interaction with the environment than traditional rigid robots. Various soft actuators have been developed, such as pneumatic artificial muscles, dielectric elastomer actuators, shape memory alloys, and hydraulic actuators [1,2]. However, a specific need within soft robotics has emerged, aiming to replicate the complex hierarchical and fibrous structure of the biological actuator par excellence, the animal skeletal muscle [3]. These linear soft actuators hold significant appeal for applications that demand biomimetic load transfer, low weight, limited dimensions, and tunable stiffness [3]. Examples include advanced surgical instruments, orthotic devices, exoskeletons, and bio-inspired robots [4]. Despite the promising results in this regard, a fundamental question is still open on how to properly connect these soft actuators to the joint to place in movement. The smooth and contractile skeletal muscles play a pivotal role in daily movements in the animal body, but their forces are transmitted to the related bones through tendons.

While skeletal muscles, with their smoothness and contractility, are the physical actuators of the animal kingdom, tendons, as complex collagenous ropes, are the stiff and elastic responsible for the muscular force transmission to the related bone segments [5]. Even if these two tissues have a similar fibrous hierarchical structure, their composition is

---

* Corresponding authors.

E-mail addresses: alberto.sensini2@unibo.it, alberto.sensini@maastrichtuniversity.nl (A. Sensini), a.zucchelli@unibo.it (A. Zucchelli).

totally different. Skeletal muscles mainly comprise fiber-like poly-nucleated cells (myofibers) that embed several parallel fibrillar units (myofibrils) structured in repeated linear sections, named sarcomeres. These structures are composed, in turn, of fibrous protein chains (actin and myosin) that, sliding over each other, generate muscular contraction [6]. Bunches of axially aligned myofibers generate the muscular fascicles that, grouped by a collagenous fibrous membrane (epimysium), constitute the muscle belly [7]. From the tendon side instead, while having a similar fibrous hierarchical arrangement compared to the muscles, the composition is entirely different. Tendons are extracellular matrix-based tissues, mainly composed of axially aligned collagen Type I fibrils and less amounts of elastin and proteoglycans [8]. Generally, each skeletal muscle lives between two tendons that are connected, in turn, at the related bony side. The muscle-to-tendon interface, called myotendinous junction (MTJ), is a complex continuous tissue gradient that reduces mechanical stress concentration [9]. The structural and mechanical differences between muscles and tendons require the design of a unique interface: the muscle contraction is intracellular, while the ECM that gives the tendon its strength is extracellular [10].

Morphologically speaking, the MTJ is not a simple three-dimensional interface between tissues, but the muscle and tendon tissues meet throughout an interface zone, creating a network of interdigitating tissue fibers. This arrangement produces a larger surface area for the adhesion of these tissues [11]. The increased surface area and the gradient of tissue composition allow a smooth transition in mechanical impedance and stresses. This compliant-to-stiff tissue decreases the risk of stress concentrations, protecting the MTJ and the surrounding tissues from potential injuries during daily life movements [11]. Looking at the microscale, the interdigitate projections of myofibers and fascicles at the MTJ often assume conical shapes [11]. This configuration is strategic to confer to the MTJ a gradient of mechanical properties passing from the tendon to the muscle tissue [12].

In the last decades, researchers have focused on trying to mimic, simulate, replace, and separately regenerate (also for soft-robotics purposes [3]) the muscle [13–16] and the tendon [17–20] tissue. In this context, electrospinning is one of the most efficient and effective techniques to regenerate and mimic muscles and tendons [3,21].

Electrospinning can scale up the production of biomimetic scaffolds and actuators for muscles and tendons by producing nanometric fibers, mimicking their extracellular matrix arrangement [21–23]. In terms of materials, polyurethane (PU) [24–27] has emerged as a viable option to mimic the softness, compliance, flexibility, and high tensile strain that are necessary for artificial muscles [26,28,29]. Similarly, nylon 6.6 (NY) [30–32] was widely investigated in the electrospinning field to mimic the mechanical performances of the tendon tissue, in particular its stiffness. Moreover, both NY and PU were widely investigated in soft robotics also for their electrostrictive properties [3,33], making these materials of high interest in the production of soft actuators.

In soft robotics, the movement of bodies is realized using rigid cables [34,35], acting as tendons and actuators, resembling muscles. The junction between the cable and the actuator is one of the most critical points for this actuation system due to the intense concentrations of stress that can cause its failure [36]. A reasonable way to mitigate the risk of ruptures is to make the junction between the actuator and cable similar to the natural MTJ. Only a few studies in this field focused on the reproduction of MTJ [11]. Ladd et al. attempted to replicate this complex interface by producing electrospun 2D mats with gradients of electrospun random nanofibers of different materials [37]. Despite the promising results, they did not obtain a continuous transition of axially aligned nanofibers as at the natural MTJ, but only random-to-aligned nanofibers. However, this configuration is far from to the organization of the natural tissue of MTJ that is thought to connect aligned-to-aligned patterns of fiber structures (i.e. myofibers and collagen fibrils). Other groups successfully realized mats with regions of random-to-aligned nanofibers (primarily for tendon/ligament-to-bone regeneration [21,38]). More recently, Tindell and co-authors developed a very

preliminarily magnetic-based method to produce random-to-aligned mats of electrospun fibers with different patterns for the regeneration of the enthesis tissue [39]. However, they were not able to match different materials together in separate regions or confer a controlled 3D structure to the scaffold. It is possible to conclude that a procedure to realize 3D aligned-to-aligned continuous junctions of nanofibers is still an open and hot challenge both for soft robotics and tissue engineering applications. Moreover, scaling up these electrospun structures to recreate an entire tendon–muscle fascicle unit remains unexplored. Thus, the need emerges for soft robotics and tissue engineering fields to develop artificial muscles and their related force transmitters (the tendons) and a valid strategy to connect them like the MTJ.

This study designs a versatile and unique workflow to produce biomimetic muscle-to-tendon interfaces for soft robotic systems entirely based on a single electrospinning process. By producing nanometric highly aligned fibers, electrospinning can scale up the production of muscles and tendons [21–23]. NY was chosen for the tendon side, while PU for the muscle one. Two different designs of artificial MTJ were realized, overlapping electrospun NY and PU mats at the MTJ with different geometries, rectangular or parallelogram-like. Mats were then rolled up, obtaining continuous biomimetic muscle–tendon fascicle-inspired bundles with their MTJs. Mats employing a rectangular overlap resulted in a flat interface, while the mats with a parallelogram-like geometry in a conical interface. Nanofibers, bundles, and junctions were characterized with scanning electron microscopy (SEM) and micro-computed x-ray tomography (microCT), while the bundles' mechanical properties were investigated using tensile and cyclic tests.

2. Materials and methods

2.1. Materials

Poly[4,4′-methylenebis(phenyl isocyanate)-alt-1,4-butanediol/di (propylene glycol)/polycaprolactone], a PU constituted by hard segments of 4,4′-methylenebis(phenyl isocyanate) (MDI) and polyether-ester soft segments, was purchased from Merck (Darmstadt, Germany). Tetrahydrofuran (THF, 99.9 %) and N,N-Dimethylformamide (DMF, 99.8 %) were supplied by Merck and mixed with PU, obtaining the following solution: 25 % (w/v) solution of PU dissolved in THF:DMF = 70/30 (v/v). Nylon 6.6 pellets, provided by DuPont (Zytel_E53 NC010, Wilmington, USA), were dissolved in a trifluoroacetic acid (TFA) (Carlo Erba, Milan, Italy) and acetone (AC) (Sigma Aldrich, Saint-Louis, USA) mixture, obtaining the following solution: 15 % (w/v) solution of Nylon 6.6 dissolved in TFA:AC = 50:50 (v/v).

2.2. Electrospun bundles preparation

A commercial electrospinning machine (Spinbow srl, Bologna, Italy) equipped with a linear sliding spinneret with four needles and a rotating drum collector was used to produce nanofibers. Four syringes carrying the polymeric solution fed the needles through PTFE tubes. The flow rate was controlled by a syringe pump (KD Scientific 200 series, Illinois, USA). The needles, connected to a high-voltage generator, were mounted on a spinneret that could slide horizontally at 1500 mm/min for both solutions. Instead, the drum collector rotated at 2500 rpm (peripheral speed = 20 m/s). The drum was covered with polyethylene (PE) coated paper (Turconi S.p.A, Ceriano Laghetto, Italy) to detach the nanofibrous mats easily. All the processes were carried out at room temperature and 30 – 40 % relative humidity.

Aiming to reproduce the structure of MTJ [9] (Fig. 1A), muscle and tendon fascicle-inspired bundles were produced separately at first. To simulate the muscle myofibrils (mean diameter up to 1 μm [40]), PU electrospun nanofibers were obtained, according to a procedure adapted from [25], by applying the following conditions: applied voltage = 23 kV; feed rate = 0.3 ml/h; needles-collector distance = 180 mm; needles inner diameter = 0.51 mm; sliding spinneret excursion = 180 mm (along
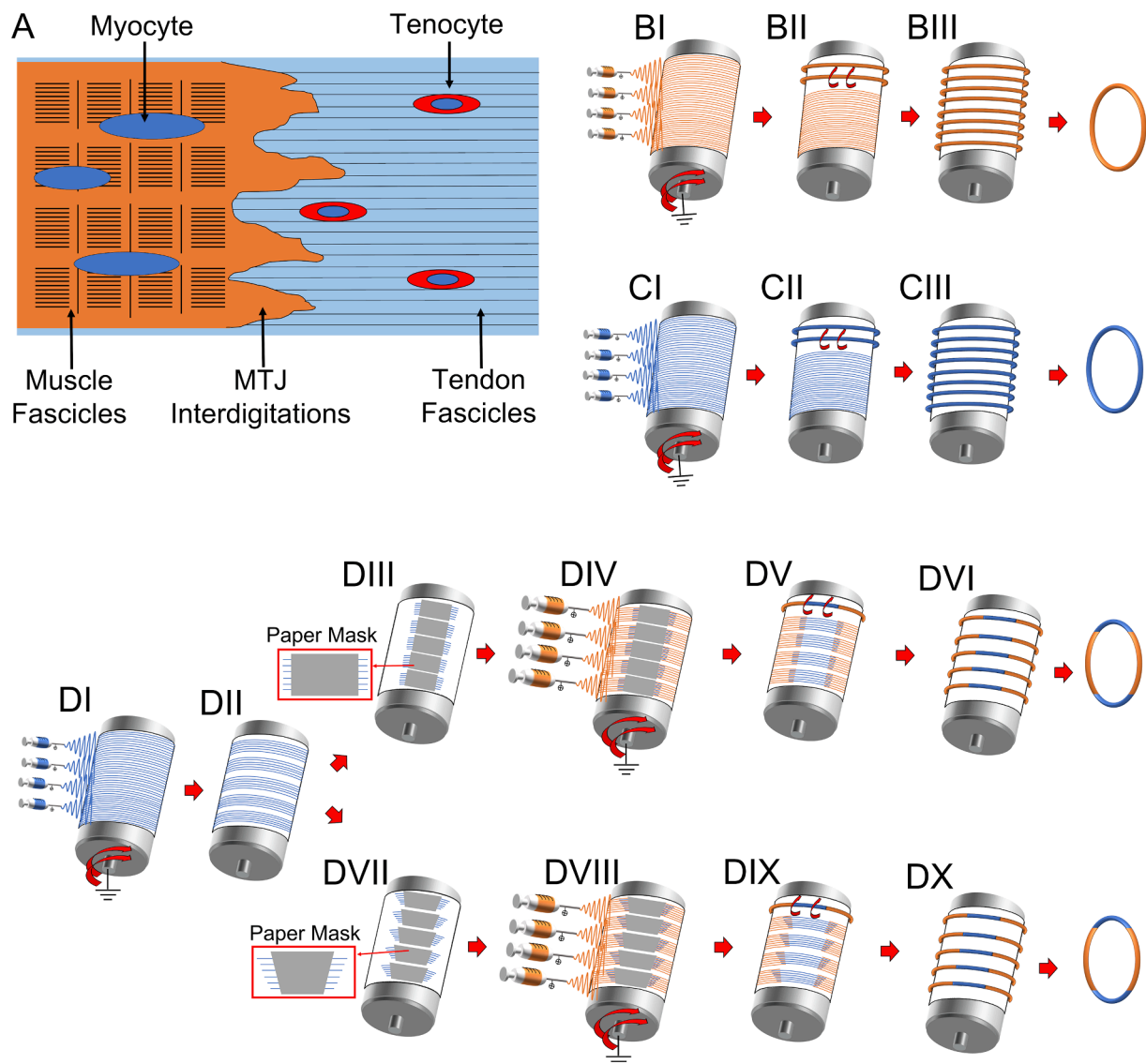
Fig. 1. MTJ structure and fabrication of bundles. A) Structure of the MTJ. B) Fabrication of the RBPU: BI) PU nanofibers electrospun on the high-speed drum collector; BII) mat cut in stripes and rolled up to obtain the bundles; BIII) bundles pulled out from the drum, obtaining RBPU. C) Fabrication of the RBNY: CI) NY nanofibers electrospun on the high-speed drum collector; CII) mat cut in stripes and rolled up to obtain the bundles; CIII) bundles pulled out from the drum, obtaining RBNY. D) Fabrication of bundles with junctions: DI) NY nanofibers electrospun on the high-speed drum collector; DII) mat cut in five stripes; DIII) stripes cut and covered with the rectangular paper masks to obtain flat junctions; DIV) PU nanofibers electrospun on the high-speed drum collector; DV) masks removed and stripes rolled up; DVI) bundles removed from the drum obtaining RBFJ; DVII) NY stripes cut and covered with the trapezoidal paper masks to obtain conical junctions; DVIII) PU nanofibers electrospun on the high-speed drum collector; DIX) masks removed and stripes rolled up; DX) bundles removed from the drum obtaining RBCJ.

the collector), for a total of 1.30 h of electrospinning. To mimic the muscle fiber/fascicles (mean diameter = 500–600 μm [3]), mats were cut into strips of 35 mm and rolled up to obtain ring-shaped bundles of PU (RBPU) (Fig. 1B).

To obtain tendon fibril-inspired nanofibers (mean diameter up to 300 nm) NY nanofibers were electrospun by applying the following conditions (adapted from [32,41]): applied voltage = 22 kV; feed rate = 0.5 ml/h; needles-collector distance = 160 mm; needles inner diameter = 0.84 mm; sliding spinneret horizontal excursion = 100 mm, for a total of 1.30 h of electrospinning. To mimic the tendon fascicles (mean diameter approximately 300 μm [8]), mats were cut in strips of 35 mm along the circumference and rolled up to obtain ring-shaped bundles of NY (RBNY) (Fig. 1C). Combining the previous procedures by electrospinning firstly NY and then PU, it was possible to produce bundle with two different materials along its length. Moreover, two junction shapes, consisting of a physical overlap of NY and PU mats, were realized to evaluate their effect on the mechanical behavior of the composite

bundle.

The first electrospinning process with NY (1.30 h with the parameters described above) produced the material for the tendon-like part of the bundle. The NY mat was cut into 35 mm-wide strips along the drum's circumference. Only five evenly spaced strips were kept, while the others were removed. Two paper masks (size = 62.5 x 35 mm) were taped over each NY strip on opposite sides of the drum (Fig. 1DIII), fixed with stripes of paper tape, to cover the mat sections that form the tendon section alone. On both sides of each paper mask, a 20 x 35 mm portion of NY mat was left uncovered, and the rest was removed. These uncovered rectangular portions form the NY component of the MTJ. A second electrospinning process with PU (1.30 h with the parameters described above) formed the fibrous portion related to the muscle (Fig. 1DIV). At the end of the process, the PU mat was kept only along the five strips identified above, leaving two sections of each strip of pure PU, four parts (the MTJ) consisting of the overlap of NY-PU, and two of NY nanofibers only. These bi-material mat stripes were obtained after removing the

paper masks protecting the NY, and the PU nanofibers remained on them as well, after having gently cut the PU stripe along the paper tape. Rolling up the strips resulted in bi-material ring-shaped bundles with four flat junctions each (RBFJ) (Fig. 1DIII-DVI).

Similarly, the conical junctions were obtained by placing trapezoidal masks (long base = 77.5 mm; short base = 47.5 mm; height = 35 mm) on the NY mats, leaving two extra sides of 20 mm each outside the masks and connecting them with a diagonal cut. In this way, the same overlap area of NY and PU nanofibers was achieved for both types of bi-material bundles, but in this latter case assuming the shape of a parallelogram. Then, ring-shaped bi-material bundles were formed by rolling up the mat from right to left and creating a conical junction (RBCJ) (Fig. 1DVII-DX) with PU nanofibers penetrating the NY ones, simulating the MTJ. This method allowed to obtain bundles with equal amounts of PU and NY.

2.3. Morphological characterization

2.3.1. SEM investigation

Specimen surfaces were observed on gold sputter-coated samples with SEM (Phenom Pro-X, Thermo Fisher Scientific, Waltham, MA, USA). ImageJ [42] was used to measure 200 diameters of NY and PU nanofibers and to investigate their distribution. The nanofibers' orientation was evaluated using the Directionality plugin of ImageJ [43]. This approach allowed estimating the number of nanofibers within a given angle from the main axis using a Local Gradient Orientation method, following a previously validated procedure [32,44]. The analysis was performed on five images (magnification: PU = 3000x; NY: 8000x) of NY and PU bundles. The nanofibers' orientation was considered equal for all the samples since the rotational speed and the electrospinning parameters were maintained constant for all the samples under investigation. The diameter of RBNY and RBPU bundles were calculated with an optical microscope (Axioskop, Zeiss, Pleasanton, CA, USA) equipped with a camera (AxioCam MRc, Zeiss, Pleasanton, CA, USA), and data were provided as the mean and standard deviation of 10 measures. For the RBFJ and RBCJ, the same procedure was performed along their length in both the NY, PU, and junction sides. After the end of cyclic tests, an additional SEM investigation, with the same methodology described above, was performed on RBNY, RBPU, RBCJ, and RBFJ to investigate the nanofibers diameters distribution and the overall structure of junctions. Moreover, a post-test orientation analysis was also performed as previously described (but using 8000x images both for PU and NY).

2.3.2. MicroCT investigation

Bundles (pure NY, pure PU, flat and conical junctions) were scanned in a microCT (Skyscan 1172, Bruker, Belgium) at a nominal resolution of 9 μm of voxel size employing no filter and with an applied x-ray tube voltage of 40 kV. The scan orbit was 180° with a rotation step of 0.2°. Image reconstructions were carried out with a modified Feldkamp algorithm using the SkyScanTM NRecon software accelerated by GPU. Moreover, a ring artifact reduction was applied. The 8-bit scans of the samples were imported in Skyscan CT-Analyser (CT-An) software to separate between NY (less X-ray opaque) and PU (more X-ray opaque) on the grey scale distribution (i.e., thresholding), to highlight them with different colors. Specific grey scale ranges were identified for NY (range: 30–130) and PU (range: 130–250) by looking at the 255 grayscale levels of the scans. Noise objects were removed from the binarized image by the despeckle operation. Volume-rendered 3D images were generated using an RGBA transfer function in Skyscan CT-Voxel (CT-Vox) software driven by the previous CT-An thresholding.

2.4. Calorimetric characterization

Differential Scanning Calorimetry (DSC) was performed using a TA Instruments Q2000 DSC apparatus equipped with a Refrigerated Cooling System (RCS90). Samples were subjected to a first heating scan in the temperature range −30 to 300 °C at a rate of 20 °C/min, followed by a quench cooling to −30 °C and a second heating scan at 20 °C/min to 300 °C.

2.5. Water contact angle

The water contact angle (WCA) was assessed at RT with a KSV CAM 101 instrument. 5 μl droplets of distilled water were employed for these measurements. The temporal evolution of the side profiles of water droplets placed on the surface of mats of aligned nanofibers was recorded within a time span of 0–30 s. Three droplets for each mat of pure NY and PU were analysed.

2.6. Mechanical characterization

2.6.1. Tensile tests to failure

The mechanical tensile characterization of the electrospun bundles (n = 5 for each sample category) was carried out with a material testing machine (Mod. 4465, Instron, Norwood, USA) with a ± 100 N load cell (Instron, Norwood, USA). The test machine worked under displacement control using a monotonic ramp to failure with a strain rate of 0.33 %/s. Bundles were tested using dedicated capstan grips (consistent with the ASTM D1414 Standard) (see Fig. S1A and Fig. 4A) and room temperature and humidity (RTH). To mimic the typical working scenario of the muscle–tendon tissue, the NY sides of the RBFJ and RBCJ were placed around the capstan. The bundles gauge length was: RBPU = 187 ± 3 mm, RBNY = 222 ± 1 mm, RBFJ = 202 ± 4 mm, RBCJ = 208 ± 1 mm. The weight of the samples was calculated using a precision balance (AS 60/220.R2, Radwag, Pol) and expressed as the mean and standard deviation of three measurements.

The force–displacement curves were converted to stress–strain graphs using two different approaches. In the first one, the apparent stress (σ_A) was calculated by dividing the force by the cross-sectional area of the specimen measured before the test, whereas in the second one, the net stress (σ_N) was used to determine the mechanical properties of the specimen independently from their porosity.

For RBFJ and RBCJ, the mean diameter and density were calculated by weighting the average on the surface area of NY and PU present on each stripe before the rolling-up phase, as follows:

$$\rho_{RBFJ|RBCJ} = (0.628 \times \rho_{NY}) + (0.372 \times \rho_{PU}) = 1.165 g/cm^3 \quad (1)$$

$$d_{RBFJ|RBCJ} = (0.628 \times d_{NY}) + (0.372 \times d_{PU}) \quad (2)$$

where 0.628 (i.e., 62.8 %) is the normalized surface before the rolling up of RBFJ and RBCJ covered by NY nanofibers, and 0.372 (i.e., 37.2 %) is the normalized surface before the rolling up, covered by PU nanofibers. Being a property of the bulk material, the density of RBFJ and RBCJ ($\rho_{RBFJ|RBCJ}$) keeps a constant value (i.e., ρ_{PU} = 1.18 g/cm^3; ρ_{NY} = 1.14 g/cm^3), whereas the diameter of the RBFJ and RBCJ ($d_{RBFJ|RBCJ}$) was calculated for each different sample.

The net stress was calculated by dividing the apparent stress by the specimens' volume fraction (v). The volume fraction (v) was calculated by using the equation:

$$\nu = w/(L \times A \times \rho) \quad (3)$$

where w is the weight of the specimen, L is the total length of the specimen, A is the cross-sectional area of the specimen and ρ is the density of the materials that constitute the bundles. The volume fraction also allowed the calculation of the percentage porosity of bundles [32] as follows:

$$Porosity(\%) = (1 - \nu) \times 100 \quad (4)$$

The following indicators were considered: yield stress (σ_Y), yield strain (ε_Y), elastic modulus (E), yield force (F_Y), failure force (F_F), failure stress (σ_F), failure strain (ε_F), stiffness (K), unit work to yield (W_Y), unit

work to failure (W$_F$). The unit work to yield and failure were evaluated with the trapezoid method.

2.6.2. Cyclic tests

The cyclic mechanical characterization of bundles was conducted at RTH on a testing machine (ElectroPuls E1000, Instron Norwood, USA), working in displacement control. Due to the different stiffnesses of the tested bundles, two load cells with different load capacities were used. Specifically, the testing machine was equipped with a $\pm$ 5 N load cell (Instron, Norwood, MA, United States) for RBPU, RBFJ, and RBCJ, while a $\pm$ 2 kN load cell (Instron, Norwood, MA, United States) was used for RBNY. The ring-shaped bundles were loaded between two dedicated custom-made 3D printed capstan grips (see Fig. S1B), that reduce stress concentrations. The cross-sectional area of the specimens (for RBFJ and RBCJ in the NY and PU regions) was evaluated as mean $\pm$ SD of 10 measurements using a digital microscope (m7915mztl 5 mega-pixel, Dino-Lite, AnMo Electronics Corp, Taipei, Taiwan). Their weights were compared as mean $\pm$ SD of 3 measurements using a precision balance (Kern ABT 100-5NM Analytical Balance). The specimens (n = 5 for each category) were tested with a pre-designed cyclic test that consists of the following steps:

i) Loading phase: the bundles were loaded at 0.33 %/s up to reach the peak of displacement set for each sample category (see next point).
ii) Cycle phase: the cyclic cyclic tests were performed by applying a sinusoidal load with a 5 mm amplitude (this value was chosen to cycle along the whole linear region of the different bundles) at 1 Hz frequency for 10,000 cycles. This package of cycles was carried out by using upper and lower limits for the values of displacement delimiting the elastic region of the previously defined sample categories. These values were identified with the results of the preliminary tensile test for each different sample category (see Section 3.4.1).
iii) Unloading phase: bundles were fully unloaded at 0 N after the 10,000 cycles and started immediately with the following package.

10 packages of 10,000 cycles were performed for a total of 100,000 cycles. Also in this case the force–displacement data were converted to apparent and net stress–strain graphs (see Section 2.6.1). The maximum and minimum peaks of force (F$_{P\_MAX}$, F$_{P\_MIN}$) and stress (apparent and net) (σ_{AP_MAX}, σ_{AP_MIN}, σ_{NP_MAX}, σ_{NP_MIN}) of the bundles were monitored during the complete cyclic tests and then showed as mean $\pm$ SD of all the specimens per each sample category. In the graphs, the total unloading phase at the end of each package was not reported to increase their readability. Moreover, the following mechanical data were also extracted:

i) To monitor the settling of the elastic modulus of bundles during different packages of cycles, for each sample, the elastic modulus was evaluated (linear regression of the last 500 points of the curve) in the first loading phase of each of the 10 packages (see Fig. S2).
ii) The incremental deformation of bundles after each package was evaluated after each first loading phase, except for the first package, in which the bundles were still not deformed by the cyclic test. Specifically, after being fully unloaded at the end of the unloading phase, the bundles were loaded again in the loading phase of the following package (see Fig. S2). The new length l$_{n+1}$ of the bundles at the n + 1 loading phase will be:

$$l_{n+1} = l_n + \Delta l \tag{5}$$

where Δl is the stretching caused by the loading phase n. By dividing for the bundles' initial length l, the equation can be rewritten in terms of strain ε:

$$\varepsilon_{n+1} = \varepsilon_n + \Delta\varepsilon \tag{6}$$

where $\Delta\varepsilon$ corresponds to the bundles' deformation over cycles, and it can be monitored with the stress–strain data: after being fully unloaded in the loading phase n, the stress of the n + 1 loading phase was equal to zero until the bundle was tensed again (stress higher than zero) at a certain value of strain as shown in Fig. S2. This value of strain was monitored for all the initial loading phases of the n + 1 packages. The evolution of the deformation during the n + 1 packages was fitted with the exponential decay equation:

$$y = ae^{bx} \tag{7}$$

where y corresponds to the deformation and x to the loading phases.

i) The mean stiffness (K$_{mean}$) and elastic modulus (E$_{mean}$) between all the bundles for each sample were evaluated every 1000 cycles inside each package, with a linear regression of the loading curve of the selected cycles.
ii) The loss of work (apparent and net) (W$_{loss}$) of bundles during the cyclic tests was evaluated every 1000 cycles inside each package as the value of the cycle of hysteresis, described as the difference between the maximum work under the (apparent and net) stress–strain curves during the loading phase and the work under the curve of the unloading phase (both calculated with the trapezoid methods).

2.7. Statistical analysis

The significance of differences of the apparent and net tensile mechanical properties of the different categories (n = 5 for each) was assessed with an ANOVA 1 with a Tukey post hoc (ns p > 0.05, *p $\leq$ 0.05, **p $\leq$ 0.01, ***p $\leq$ 0.001, ****p $\leq$ 0.0001). Instead, the comparison between the apparent and net tensile mechanical properties of the same sample categories (i.e. RBPU, RBNY, RBFJ, and RBCJ) was assessed with a ratio-paired parametric *t*-test. Moreover, the significance of differences of the apparent and net cyclic mechanical properties, during each package, between the different sample categories was assessed with an ANOVA 1 with a Tukey post hoc (ns p > 0.05, *p $\leq$ 0.05, **p $\leq$ 0.01, ***p $\leq$ 0.001, ****p $\leq$ 0.0001).

3. Results and discussion

3.1. Morphology of bundles − SEM

The SEM investigation revealed that all the PU and NY bundles' nanofibers as spun (before cyclic tests = BC) were homogeneous, smooth, continuous, and with no defects, such as beads. The diameter (d) of PU nanofibers was d$_{PU-BC}$ = 0.91 $\pm$ 0.34 µm with a marked waviness (Fig. 2A, 2M), similar to the skeletal muscles myofibrils [7,40,45] and in line with other studies on electrospun PU nanofibers [46–48]. Notably, some groups of PU nanofibers appeared stuck together (Fig. 2B). The NY nanofibers instead, had a diameter of d$_{NY-BC}$ = 0.24 $\pm$ 0.05 µm with a reduced waviness and fully separated each other (Fig. 2B and 2M), mimicking the tendon collagen fibrils [8,49]. Similarly, RBPU, RBNY, and the PU and NY sides of RBFJ and RBCJ, resembled the skeletal muscle fibers-fascicles [7,40,45] and the tendon collagen fascicles [8,49].

All the bundles were homogeneous with a diameter of the RBPU and the PU side of the bi-material bundles of 605 $\pm$ 20 µm (Fig. 2D), while for RBNY and the NY side of the bi-material bundles, it was 350 $\pm$ 4 µm (Fig. 2C). The RBFJ had a mean diameter of 501 $\pm$ 22 µm (Fig. 2G) while the RBCJ of 513 $\pm$ 29 µm (Fig. 2H).

After the removal from the drum collector (drum circumference 471 mm), all the bundles showed different percentages of shrinkage, strongly dependent on the PU side of bundles, which was 21 $\pm$ 1 % for the RBPU, 5.6 $\pm$ 0.3 % for RBNY, 14 $\pm$ 2 % for the RBFJ and 12 $\pm$ 0.4 %
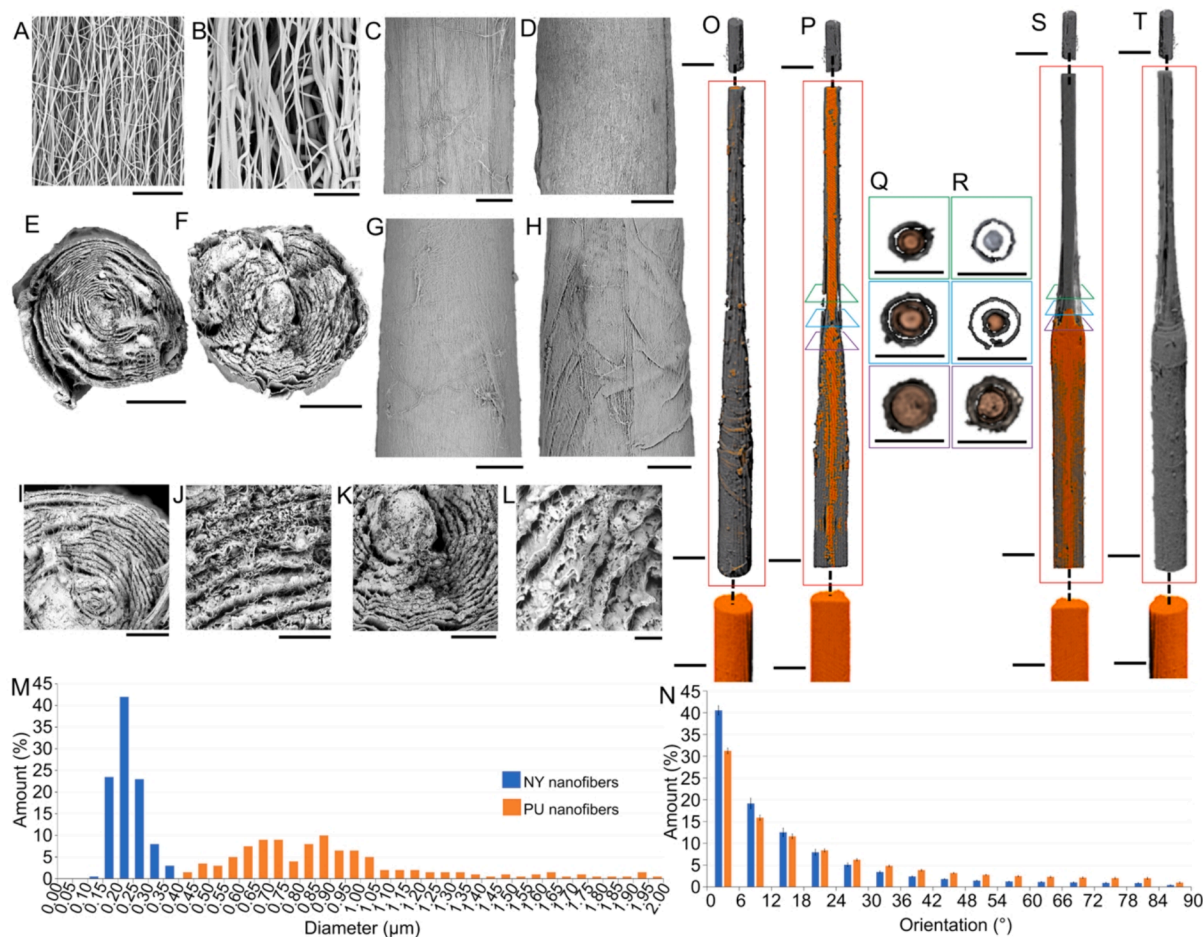
Fig. 2. SEM and microCT investigations on bundles. A) NY nanofibers (magnification = 10000x, scalebar = 8 μm); B) PU nanofibers (magnification = 10000x, scalebar = 8 μm); C) Typical RBNY and NY side of bi-material bundles (magnification = 600x, scalebar = 100 μm); D) Typical RBPU and PU side of bi-material bundles (magnification = 380x, scalebar = 200 μm); E) Cross-section of RBFJ (magnification = 300x, scalebar = 200 μm); F) Cross-section of RBCJ (magnification = 300x, scalebar = 200 μm); G) Overview of RBFJ at the junction side (magnification = 260x, scalebar = 150 μm); H) Overview of RBCJ at the junction side (magnification = 260x, scalebar = 150 μm); I) Zoom-in of the cross-section of a RBFJ (magnification = 750x, scalebar = 100 μm); J) Zoom-in of the layers of the cross-section of a RBFJ (magnification = 4000x, scalebar = 20 μm); K) Zoom-in of the cross-section of a RBCJ (magnification = 1000x, scalebar = 80 μm); L) Zoom-in of the layers of the cross-section of a RBCJ (magnification = 4500x, scalebar = 10 μm); M) Diameter distribution of NY and PU nanofibers; N) Orientation of the nanofibers of NY and PU of bi-material bundles (axial orientation = 0°; transversal orientation = 90°); O) MicroCT of RBCJ (NY: grey, PU: orange); P) MicroCT of RBCJ internal volume (NY: grey, PU: orange); Q) MicroCT transversal sections of a conical junction (NY: grey, PU: orange); R) MicroCT transversal sections of a flat junction (NY: grey, PU: orange); S) MicroCT of RBFJ internal volume (NY: grey, PU: orange); T) MicroCT of RBFJ (NY: grey, PU: orange) (for all microCT images scalebar = 500 μm).

for the RBCJ; reaching a final length of 374 ± 6 mm for the RBPU, 445 ± 2 mm for the RBNY, 403 ± 8 mm for the RBFJ and 416 ± 2 mm for the RBCJ.

The weight of bundles was 49 ± 2 mg for the RBPU, 12 ± 1 mg for the RBNY, 44 ± 3 mg for the RBFJ, and 43 ± 4 mg for the RBCJ, while the volume fraction (ν) was 0.39 ± 0.02 for the RBPU, 0.24 ± 0.02 for the RBNY, 0.48 ± 0.05 for the RBFJ and 0.44 ± 0.08 for the RBCJ. The porosity of bundles instead was 61 ± 2 % for the RBPU, 76 ± 2 % for the RBNY, 52 ± 5 % for the RBFJ, and 56 ± 8 % for the RBCJ.

As expected, the directionality analysis on the PU and NY nanofibers of bundles (Fig. 2N) revealed a preferential axial orientation with a biomimetic dispersion on the transversal side. This behavior was consistent with muscle myofibrils and collagen fibrils in muscle and tendon fascicles [7,50]. In particular, the PU nanofibers aligned in the range 0° − 18° was 59 ± 2 %, and 5.0 ± 0.6 % were oriented in the range 78° − 90°. Conversely, the NY nanofibers oriented in the range 0° − 18° was 72 ± 3 % while just 2.2 ± 0.3 % were found in the range 78° − 90°. These results were consistent with the higher shrinkage produced by the bundles of PU (and the PU regions of RBFJ|RBCJ) compared to the NY ones, as confirmed by previous works on similar

electrospun nanofibers [25,32,41]. Focusing on the junctions, instead, their external morphology showed a progressive reduction of diameter passing from the junction region, characterized by overlapped layers of PU and NY nanofibers (Fig. 2J, L), up to the NY side. Moreover, looking at their SEM sections, the RBFJ (Fig. 2E) showed a continuous concentric alternation of NY and PU layers of nanofibers, while in the RBCJ (Fig. 2F) was visible, an internal core of PU nanofibers surrounded by continuous layers of NY and PU nanofibers. After the cyclic tests (AC) (Fig. 3), inside RBNY and in both the NY sides of bi-material bundles, groups of nanofibers compacted each other during the test (Fig. 3A), producing some "micro-bundles" (diameters = 1.15 ± 0.39 μm) that globally contributed to the stiffening of RBNY and bi-material ones. Conversely, this phenomenon was not visible in the PU nanofibers (Fig. 3B). After the cyclic tests, no macroscopic morphological differences were detected in RBPU and RBNY (Fig. 3C–D), as well as in the flat (Fig. 3E) and conical (Fig. 3F) junctions of bi-material bundles. The post cyclic test orientation analysis revealed that NY nanofibers of RBNY (range 0° − 18°: 68 ± 6 %; range 78° − 90°: 3.3 ± 0.4 %; $d_{RBNY-AC}$ = 0.20 ± 0.06 μm), RBFJ (range 0° − 18°: 74 ± 4 %; range 78° − 90°: 2.4 ± 0.4 %; $d_{RBFJNY-AC}$ = 0.21 ± 0.05 μm) and RBCJ (range 0° − 18°: 69 ±
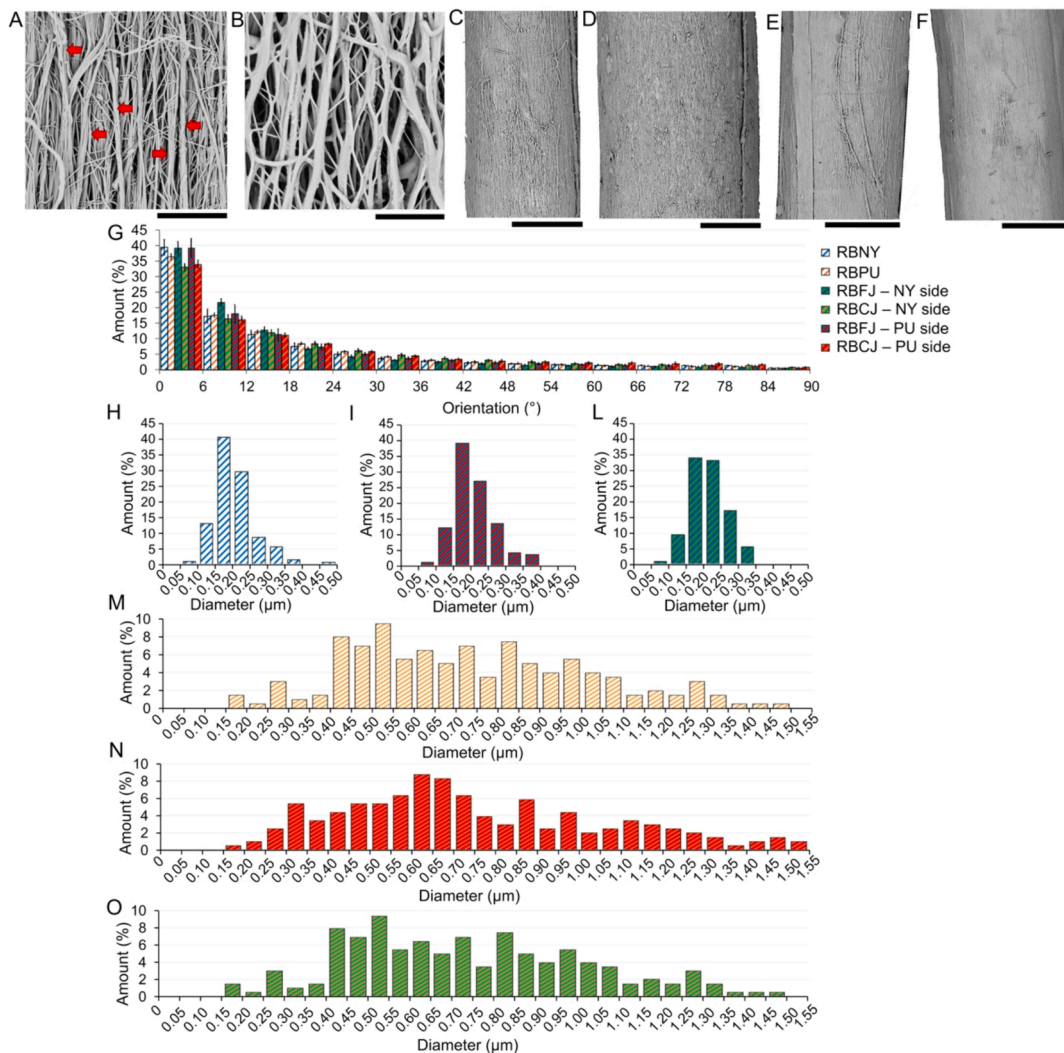
Fig. 3. Morphological investigations on bundles after cyclic tests. A) NY nanofibers (magnification = 10000x, scalebar = 8 μm; red arrows highlight the "micro-bundles" produced during tests); B) PU nanofibers (magnification = 10000x, scalebar = 8 μm); C) RBNY (magnification = 260x, scalebar = 200 μm); D) RBPU (magnification = 260x, scalebar = 200 μm); E) RBFJ at the junction side, (magnification = 260x, scalebar = 200 μm); F) RBCJ at the junction side (magnification = 260x, scalebar = 200 μm); G) Orientation of the nanofibers of the bundles after the cyclic tests (axial orientation = 0°; transversal orientation = 90°); H) Diameter distribution of the nanofibers of the RBNY after the cyclic tests; I) Diameter distribution of the nanofibers of the RBFJ, on the NY side, after the cyclic tests; L) Diameter distribution of the nanofibers of the RBCJ, on the NY side, after the cyclic tests; M) Diameter distribution of the nanofibers of the RBPU after the cyclic tests; N) Diameter distribution of the nanofibers of the RBFJ, on the PU side, after the cyclic tests; O) Diameter distribution of the nanofibers of the RBCJ, on the PU side, after the cyclic tests.

8 %; range 78° − 90°: 3.2 ± 0.6 %; $d_{RBCJNY-AC}$ = 0.21 ± 0.06 μm) substantially maintained their orientation (Fig. 3G). The PU nanofibers instead, both for RBPU (range 0° − 18°: 66 ± 2 %; range 78° − 90°: 2.9 ± 0.4 %; $d_{RBPU-AC}$ = 0.73 ± 0.28 μm), RBFJ (range 0° − 18°: 61 ± 3 %; range 78° − 90°: 4.0 ± 0.5 %; $d_{RBFJPU-AC}$ = 0.73 ± 0.28 μm) and RBCJ (range 0° − 18°: 61 ± 3 %; range 78° − 90°: 4.4 ± 0.9 %; $d_{RBCJPU-AC}$ = 0.74 ± 0.31 μm) showed a slightly increment of alignment compared to the as spun ones (Fig. 3G). The PU nanofibers after test resulted also more detatched each other compared to the as spun ones. Also the morphology of junctions was maintained after the cyclic test (Fig. 3). All the different families of bundles (RBNY, RBPU, RBFJ and RBCJ) showed a reduction of the diameters of both their NY and PU nanofibers (around 12 % for NY and around 19 % for PU) (Fig. 3H-O), probably caused by local internal reorganizations of bundles, but without any visible break. These findings promote a fast, stable and continuous transmission of load between the two regions of bi-material bundles, reducing consequently the delay in the operation, suggesting their suitability for soft robotics applications.

3.2. Morphology of bundles − microCT

Previous analysis and considerations were confirmed by the microCT scans of the RBFJ (Fig. 2S, 2T) and RBCJ (Fig. 2O, 2P). The microCT scans also allowed to verify the full-field internal structure of junctions and the pure NY and PU sides. The microCT analysis detected the global grayscale alteration depending on the concentration of PU and NY nanofibers. The SEM and microCT images of RBCJ confirmed their close mimicry with the natural structure of the MTJ, where the muscle fibers interdigitate inside the tendon fascicle. However, considering the voxel size adopted (9 μm), it was not possible to discriminate the nanofibers and the overlapped layers of the wrapped-up mats [9]. Moreover, looking at the external surface of both junctions, only NY nanofibers were visible until the PU side of bundles was reached, further confirming the biomimicry of these structures with the natural tissue (Fig. 2G, 2H, 2O, and 2T). In fact, tendon fascicles incorporate the muscle ones progressively becoming endomysium/perimysium [9,45].

3.3. Electrospun mats wettability

The behavior of a typical water droplet for each sample is depicted in Fig. S3. The PU mat, consisting of aligned nanofibers, exhibited a WCA of $114° \pm 6°$, which remained nearly consistent throughout the observation period. In contrast, the WCA values for NY samples slightly declined over time, registering a mean WCA of $76° \pm 10°$ over 30 s, showing a higher hydrophilicity compared to the PU ones. However, despite the slightly higher hydrophilicity of NY nanofibers than the PU

ones, both materials demonstrated a WCA suitable for their potential applicability in soft robotics.

3.4. Mechanical properties of bundles

3.4.1. Tensile properties

The mechanical tensile properties of bundles are summarized in Fig. 4, Table S1, Table S2, and Table S3. In particular, the force–displacement, force-strain, and stress–strain curves of RBNY showed a
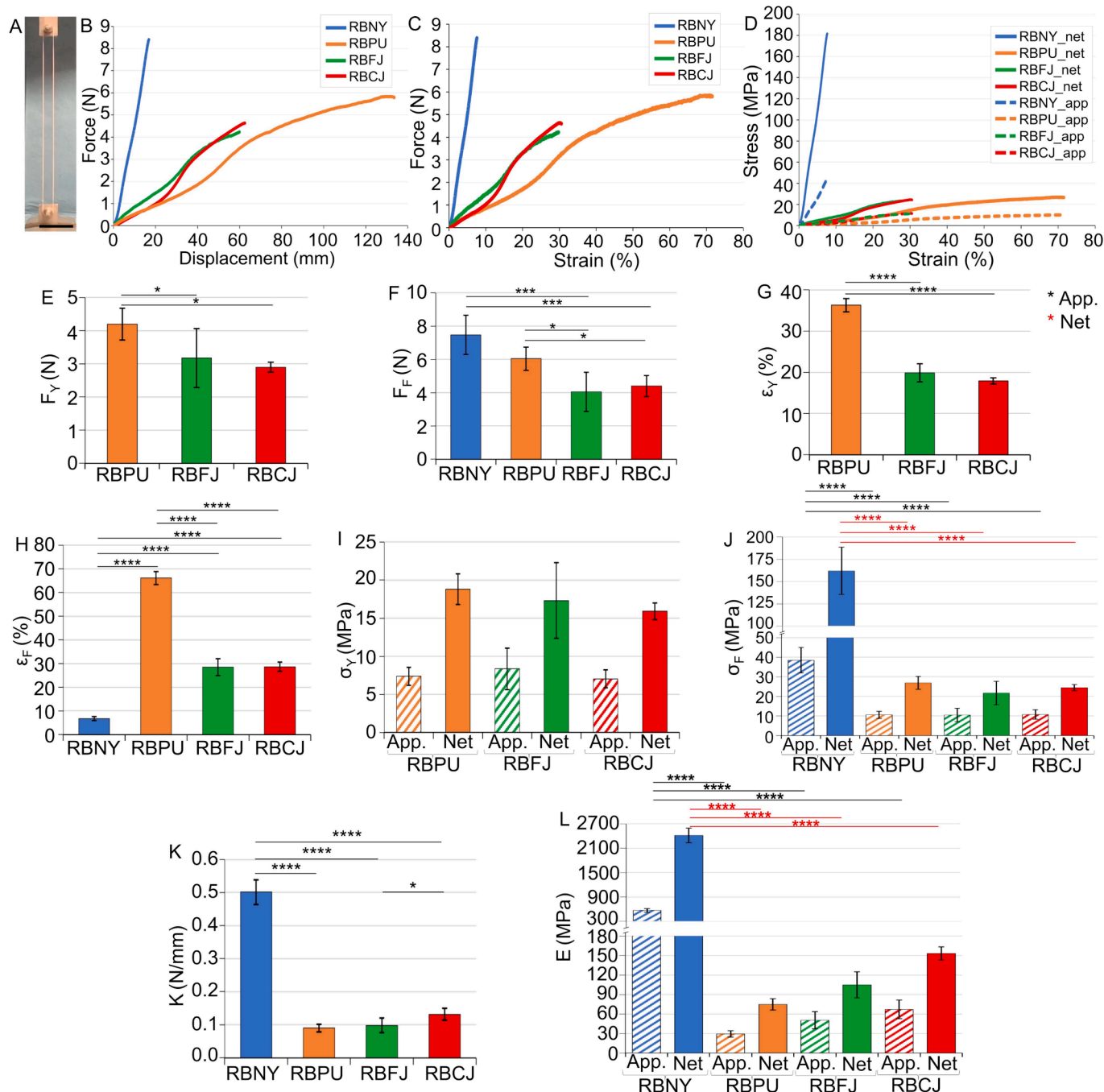

Fig. 4. Mechanical tensile properties of bundles (striped lines/bars = apparent properties; solid lines/bars = net properties). A) Setup for the tensile test (scale bar = 20 mm); B) typical force–displacement curves of bundles; C) Typical force-strain curves of bundles; D) Typical stress–strain curves of bundles; E) Yield force; F) Failure force; G) Yield strain; H) Failure strain; I) Yield stress; J) Failure stress; K) Stiffness; L) Elastic modulus. The significance of differences between the different categories of bundles in terms of apparent and net mechanical properties was assessed with an ANOVA 1 test followed by a Tukey post doc. The mean and standard deviation are plotted, and statistical significance is evaluated using one-way ANOVA followed by Tukey's multiple comparisons (ns $p > 0.05$, *$p \leq 0.05$, **$p \leq 0.01$, ***$p \leq 0.001$, ****$p \leq 0.0001$; black asterisks = apparent; red asterisks = net).

nonlinear fragile behavior, while the RBPU showed a nonlinear ductile behavior with large deformations. The samples with junctions, RBFJ and RBCJ, showed a nonlinear ductile behavior with intermediate values between RBNY and RBPU (Fig. 4B–D). All the bundles showed an initial toe region (less extended in RBNY than RBPU, RBFJ, and RBCJ) similar to the natural tissue counterpart [51–53]. The RBNY had the less extended toe region (~2% strain), similar to the ones of natural tendon fascicles [51], RBPU conversely had the longer toe region (~26 % strain), similar to the natural muscle fiber/fascicles [52], while again both the RBFJ and RBCJ toe regions (~15 % and ~ 14 % strain respectively) resulted similar to the ones of natural MTJ [52]. The RBNY had a failure force of $F_F = 7.5 \pm 1.2$ N ($\varepsilon_F = 6.8 \pm 0.9$ %), the RBPU of $F_F = 6.0 \pm 0.7$ N ($\varepsilon_F = 66 \pm 3$ %), the RBFJ of $F_F = 4.0 \pm 1.2$ N ($\varepsilon_F = 28 \pm 4$ %) and the RBCJ of $F_F = 4.4 \pm 0.6$ N ($\varepsilon_F = 29 \pm 2$ %) with no significant differences between the two junctions (Fig. 4F, H).

The contribution of the NY sides caused a reduction of 58 % and 56 % of the failure strain of RBFJ and RBCJ compared to the RBPU, while the contribution of the PU side produced a significant reduction of the junction's failure force. In terms of yielding forces/strains, the RBPU had $F_Y = 4.2 \pm 0.5$ N ($\varepsilon_Y = 36 \pm 2$ %), the RBFJ of $F_Y = 3.2 \pm 0.9$ N ($\varepsilon_Y = 20 \pm 2$ %), and the RBCJ of $F_Y = 2.9 \pm 0.2$ N ($\varepsilon_Y = 18 \pm 0.8$ %). In this case, the presence of NY caused a reduction of the yield strain of RBFJ of 44 % and for the RBCJ of 50 % and a similar trend of statistics previously described (Fig. 4E, G, and Table S2).

In terms of yield stress, the one of RBPU was $\sigma_{AY} = 7.4 \pm 1.2$ MPa ($\sigma_{NY} = 19 \pm 2$ MPa), the one of RBFJ was $\sigma_{AY} = 8.4 \pm 2.7$ MPa ($\sigma_{NY} = 17 \pm 5$ MPa), and the one of RBCJ was $\sigma_{AY} = 7.0 \pm 1.2$ MPa ($\sigma_{NY} = 16 \pm 1$ MPa) with no significant differences between the different categories (Fig. 4I). This fact confirms that the presence of NY did not compromise the ductility of bundles but only their stiffness. The failure stress instead for RBNY was $\sigma_{AF} = 38 \pm 7$ MPa ($\sigma_{NF} = 162 \pm 27$ MPa), for RBPU $\sigma_{AF} = 11 \pm 2$ MPa ($\sigma_{NF} = 27 \pm 3$ MPa), for RBFJ $\sigma_{AY} = 10 \pm 3$ MPa ($\sigma_{NF} = 22 \pm 6$ MPa), and for RBCJ $\sigma_{AF} = 11 \pm 2$ MPa ($\sigma_{NF} = 24 \pm 2$ MPa), with significant differences only with the respect of RBNY (Fig. 4J).

Concerning the stiffness of bundles, for RBNY it was $K = 0.50 \pm 0.04$ N/mm, for RBPU $K = 0.09 \pm 0.01$ N/mm, for RBFJ $K = 0.10 \pm 0.02$ N/mm and for RBCJ $K = 0.13 \pm 0.02$ N/mm. Interestingly, a significant difference was detected between the stiffness of RBFJ and RBCJ (p = 0.1659), and the differences increased even more between the RBNY and the other bundle categories (Fig. 4K). This demonstrates the ability of the conical junction to induce a stiffening effect to the RBCJ.

The elastic modulus was strongly dependent on the junction's shape. In fact, for RBNY it was $E_A = 573 \pm 45$ MPa ($E_N = 2416 \pm 180$ MPa), for RBPU $E_A = 29 \pm 5$ MPa ($E_N = 73 \pm 9$ MPa), for RBFJ $E_A = 50 \pm 13$ MPa ($E_N = 105 \pm 20$ MPa), and for RBCJ $E_A = 67 \pm 14$ MPa ($E_N = 153 \pm 10$ MPa), confirming the ability of RBCJ to increase the elastic modulus of bundles more than RBFJ (Fig. 4L).

Up to the yielding point, RBPU was able to store more work ($W_{AY} = 0.001 \pm 0.0002$ J/mm^3; $W_{NY} = 0.003 \pm 0.0004$ J/mm^3) compared to RBFJ ($W_{AY} = 0.0008 \pm 0.0003$ J/mm^3; $W_{NY} = 0.002 \pm 0.0006$ J/mm^3) and RBCJ ($W_{AY} = 0.0005 \pm 0.0001$ J/mm^3; $W_{NY} = 0.001 \pm 0.0001$ J/mm^3) (Table S1, Table S2, and Table S3). Interestingly, for the apparent work to failure, RBNY ($W_{AF} = 0.001 \pm 0.0003$ J/mm^3; $W_{NF} = 0.005 \pm 0.001$ J/mm^3), RBFJ ($W_{AF} = 0.002 \pm 0.001$ J/mm^3; $W_{NF} = 0.003 \pm 0.001$ J/mm^3), and RBCJ ($W_{AF} = 0.001 \pm 0.0004$ J/mm^3, $W_{NF} = 0.003 \pm 0.0005$ J/mm^3) had similar values without significant differences while RBPU ($W_{AF} = 0.004 \pm 0.0007$ J/mm^3; $W_{NF} = 0.01 \pm 0.001$ J/mm^3) were able to store significant more work (p < 0.0001) before failure compared to the other categories (Table S1, Table S2, and Table S3).

The net mechanical properties of bundles, avoiding the contribution of their internal empty spaces, were generally two–three times higher (and significantly different) than the apparent ones (see Fig. 4 and Table S3). Concerning the overall mechanical data of bundles, even if the values differ in some points compared to the natural tissue counterpart data found in the literature [51–53], their mechanical behavior

and trends in mechanical properties agree with the mechanics expected to simulate these tissues. Furthermore, the net mechanical properties of RBCJ, in terms of elastic modulus and failure strain ($E_N = 153 \pm 10$ MPa; $\varepsilon_F = 29 \pm 2$ %) (Fig. 4 and Table S1), were in the same range of the ones of natural pig MTJ found in literature (i.e. $E_N = 126.05 \pm 40.42$ MPa; $\varepsilon_F = 40 \pm 9$ %) [52].

3.4.2. Cyclic tests

A skeletal and artificial muscle's main passive mechanical characteristic is its ability to withstand several load cycles without damage. The main task of the MTJ is to connect a soft tissue (such as the muscle/soft actuator) and a much stiffer tissue (such as the tendon tissue/joint). This fact guarantees a constant tone to the kinematic chain, withstanding cyclic loads, and simultaneously reduces the stresses produced. For these reasons, a cyclic test, consisting of 10 packages of 10,000 cycles each, was performed using a typical physiological walking frequency (i.e., 1 Hz) [54]. Some results in this section may differ from the mechanical properties reported in the tensile tests. This fact is due to the viscoelastic properties of these materials, which result in slightly different mechanical properties depending on the strain rate employed (5 %/s for cyclic tests, corresponding to a frequency of 1 Hz, versus 0.33 %/s for tensile tests).

Since muscles and tendons work by cycling within a linear elastic region, cyclic tests were designed to do the same, setting upper and lower displacement limits due to cycle in a linear region between the end of the toe region and before the yield point. Specifically, RBNY = 8–13 mm, RBPU = 45–50 mm, and RBFJ/RBCJ = 26–31 mm.

The results obtained from the cyclic phase of the cyclic test are shown in Fig. 5. Specifically, the mean values of maximum and minimum peaks of force and stress (apparent and net) are shown in Fig. 5B–G, while the values of stiffness and elastic modulus evaluated every 1000 cycles are reported in Fig. 5H and I (mean values of loss of work are shown in Fig. S5). Mean ± SD of the cyclic mechanical properties evaluated between the 10 packages are reported in Table S4, while in Fig. S6, Table S5, and Table S6, the mean ± SD of these values are reported for each package.

As expected, for RBPU, RBFJ, and RBCJ, all the cyclic properties showed a decay (emphasized in the first package) up to the fourth package and then tent to progressively stabilize their decay (Fig. 5B–I, Fig. S5 Fig. S6 and Tables S4-S6). Conversely and surprisingly, RBNY, after a fast decay in the first 10,000 cycles of the first package, produced a progressive force/stress hardening up to the third package for the minimum/maximum values of the mechanical properties (i.e. mean ± SD peaks at the third package: $F_{P\_MIN} = 0.71 \pm 0.42$ N; $F_{P\_MAX} = 5.2 \pm 0.9$ N; $\sigma_{AP\_MIN} = 3.4 \pm 2.0$ MPa; $\sigma_{AP\_MAX} = 25.1 \pm 4.0$ MPa; $\sigma_{NP\_MIN} = 13.0 \pm 7.4$ MPa; $\sigma_{NP\_MAX} = 96 \pm 14$ MPa) then they maintained mean minimum peaks of $F_{P\_MIN} = 0.7 \pm 0.1$ N and $\sigma_{AP\_MIN} = 3.3 \pm 0.5$ MPa ($\sigma_{NP\_MIN} = 12 \pm 2$ MPa), as well as maximum values of $F_{P\_MAX} = 5.2 \pm 0.1$ N and $\sigma_{AP\_MAX} = 25 \pm 0.4$ MPa ($\sigma_{NP\_MAX} = 96 \pm 1.6$ MPa), up to the end of the test. This amplified the superior mechanical properties of RBNY compared to the other categories (Fig. S6 and Table S6).

A previous stress hardening effect was detected on nylon 6.6 monolithic filaments during stress-relaxation tests [55] but, to the best of our knowledge, on nylon 6.6 electrospun nanofibers, this phenomenon has not yet been reported in the literature. The stress hardening phenomenon is not related to a change in the crystallinity of NY, as demonstrated by comparing the DSC curve before and after the cyclic tests (Fig. S4), which showed an almost identical calorimetric behavior of the materials. We have previously demonstrated that NY fibers with a high molecular orientation and fibrillar crystalline structure elongated in the axial direction were obtained through electrospinning [56]. It can be conceivably hypothesized that an increase in crystalline orientation occurs during stress application to the fibers, which might justify the hardening phenomenon. Moreover, the post cyclic tests SEM investigation (Fig. 3) revealed that, inside RBNY and in both the NY sides of RBCJ and RBFJ, groups of nanofibers compacted each other producing sorts of
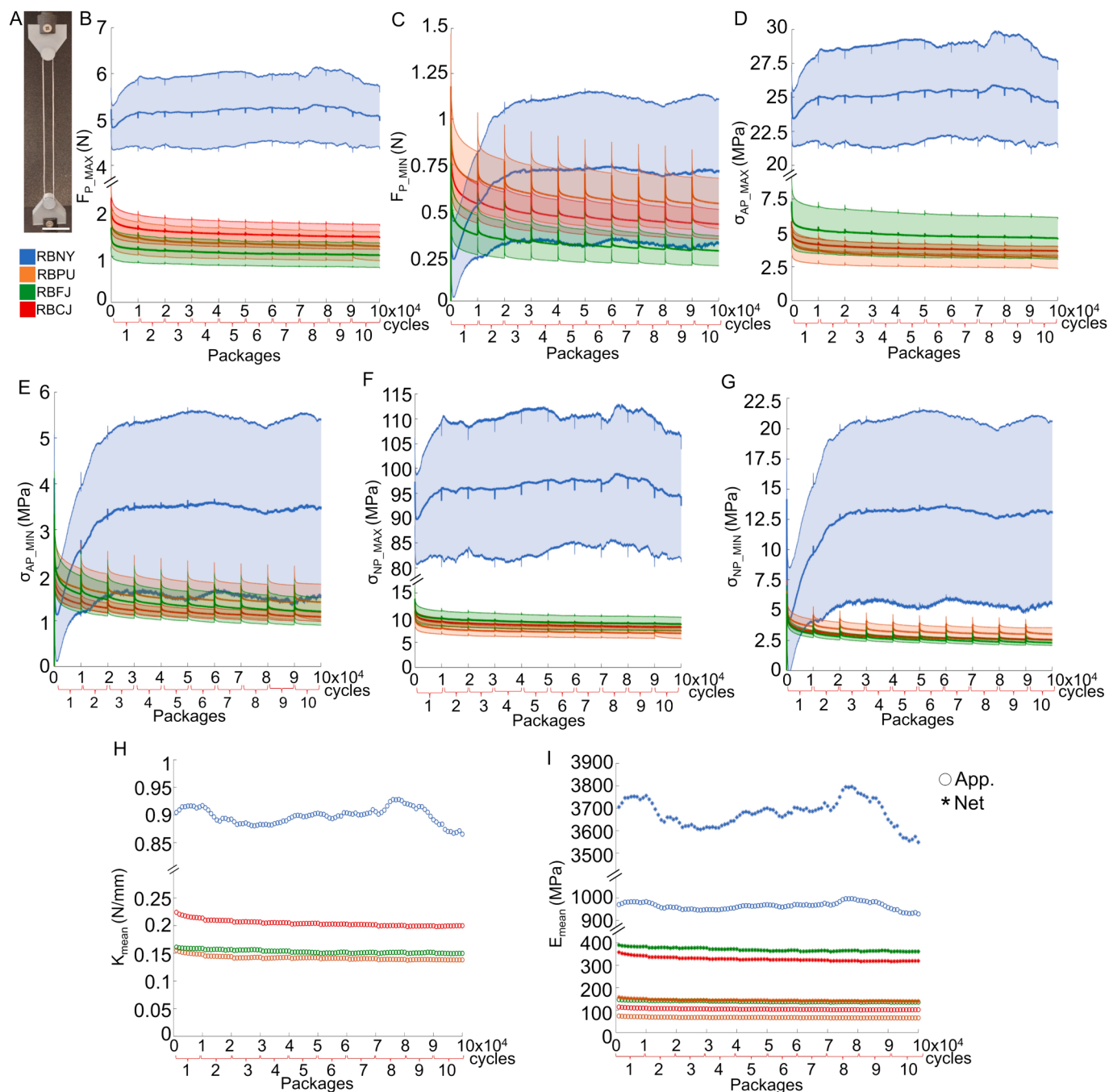
Fig. 5. Cyclic properties of bundles. The continuous lines represent the average values, while the shaded areas the related standard deviations: A) Setup for cyclic tests (scale bar = 20 mm); B) Mean ± SD maximum peaks of force of bundles; C) Mean ± SD minimum peaks of force of bundles; D) Mean ± SD maximum peaks of apparent stress of bundles; E) Mean ± SD minimum peaks of apparent stress of bundles; F) Mean ± SD maximum peaks of net stress of bundles; G) Mean ± SD minimum peaks of net stress of bundles. H) Stiffness of bundles evaluated every 1000 cycles during the cyclic tests; I) Elastic modulus (apparent and net) of bundles evaluated every 1000 cycles during the cyclic tests (circles = apparent; asterisks = net).

"micro-bundles" that globally contributed to the stiffening of NY both in pure bundles and in the bi-material ones. These findings further support the capability of junctions and bi-material bundles to dampen the stress-hardening effect of NY nanofibers.

The RBPU showed intermediate values of mean maximum peaks of force ($F_{P\_MAX} = 1.3 \pm 0.07$ N) compared to the RBCJ ($F_{P\_MAX} = 1.5 \pm 0.1$ N) and RBFJ ($F_{P\_MAX} = 1.1 \pm 0.05$ N) (Fig. 5 and Fig. S6 and Table S6) (Table S4 and Table S5). Conversely, RBPU were able to maintain higher levels of mean minimum peaks of force ($F_{P\_MIN} = 0.6 \pm 0.06$ N) if compared to the RBCJ ($F_{P\_MIN} = 0.5 \pm 0.05$ N) and RBFJ ($F_{P\_MIN} = 0.3 \pm 0.04$ N) (Fig. 5 and Fig. S6 and Table S6) (Table S4 and Table S5). In

terms of mean maximum peaks of stress, RBPU showed the lowest values ($\sigma_{AP\_MAX} = 3.3 \pm 0.2$ MPa; $\sigma_{NP\_MAX} = 7.2 \pm 0.4$ MPa) in comparison with RBFJ ($\sigma_{AP\_MAX} = 4.9 \pm 0.2$ MPa; $\sigma_{NP\_MAX} = 9.2 \pm 0.1$ MPa) and RBCJ ($\sigma_{AP\_MAX} = 3.9 \pm 0.2$ MPa; $\sigma_{NP\_MAX} = 8.2 \pm 0.1$ MPa).

The higher maximum stress values for the junctions were due to the contribution of the NY side of the bundles, where the RBCJ showed lower peaks with respect to RBFJ, demonstrating to dampen better the stress hardening of the NY side. The RBPU showed instead the higher values of mean minimum peaks of stress ($\sigma_{AP\_MIN} = 1.5 \pm 0.1$ MPa; $\sigma_{NP\_MIN} = 3.3 \pm 0.2$ MPa) in comparison with RBFJ ($\sigma_{AP\_MIN} = 1.4 \pm 0.2$ MPa; $\sigma_{NP\_MIN} = 2.6 \pm 0.3$ MPa) and RBCJ ($\sigma_{AP\_MIN} = 1.2 \pm 0.1$ MPa;

$\sigma_{\text{NP\_MIN}} = 2.8 \pm 0.3$ MPa) (Fig. S6 and Table S6) (Table S4 and Table S5).

Due to elastic nature of PU, RBPU also showed lowest mean levels of stiffness, elastic moduli (K = 0.14 ± 0.003 N/mm; $E_A = 67 \pm 1.7$ MPa; $E_N = 143 \pm 3.6$ MPa) and loss of work ($W_{\text{loss\_A}} = 0.000005 \pm 0.0000003$ J/mm^3; $W_{\text{loss\_N}} = 0.000008 \pm 0.0000002$ J/mm^3) compared with the other categories (Figs. 4, 5 Fig. S5,Fig. S6 and Tables S4, S5). Interestingly, RBCJ were able to produce and maintain higher mean levels of stiffness and a lower mean level of loss of work (K = 0.2 ± 0.005 N/mm; $W_{\text{loss\_A}} = 0.0000054 \pm 0.0000002$ J/mm^3; $W_{\text{loss\_N}} = 0.000017 \pm 0.0000006$ J/mm^3) compared to RBFJ (K = 0.15 ± 0.003 N/mm; $W_{\text{loss\_A}} = 0.0000077 \pm 0.0000002$ J/mm^3; $W_{\text{loss\_N}} = 0.000020 \pm 0.0000006$ J/mm^3) (Fig. 5, Fig. S5, Fig. S6 and Tables S4, S5) suggesting a beneficial increment in stiffness caused by the NY side while maintaining a reduced hysteresis more similar to the PU side. The RBFJ, conversely, showed higher mean levels of elastic moduli ($E_A = 139 \pm 3$ MPa; $E_N = 370 \pm 8$ MPa) when compared to RBCJ ($E_A = 104 \pm 3$ MPa; $E_N = 327 \pm 9$ MPa), confirming the tendency of RBCJ to produce lower levels of stress during the cyclic test (Fig. 5, Fig. S6 and Tables S4, S5).

Moreover, the standard deviations of RBFJ resulted higher than the RBCJ ones, suggesting a reduction of the damping effect of NY sides in this junction configuration. These data suggest the ability of the RBCJ to reduce the stress concentrations caused by the passage from NY to PU as the natural MTJ does [11,52].

Notably, the net mechanical properties of bundles during the cyclic tests in the elastic region closely matched the ones of tendon fascicles [51], muscle fibers/fascicles [57], and MTJ [11,52] reported in the literature.

The mean values of the elastic moduli of bundles during the cyclic tests were higher compared to the ones of the bundles during the tensile tests due to the higher strain rate of the cyclic tests and the progressive compacting of the nanofibers (i.e. for RBNY = 68 %, for RBPU = 131 %, for RBFJ = 178 %, for RBCJ = 55 %) (Fig. 5I and Table S4).

In Fig. 6 are shown the typical shape of the 10 loading phases of the cyclic test and the evolution of the deformation plotted at every n + 1 loading phase. Specifically, Fig. 6A–D show the apparent stress–strain plot (the net stress–strain plots are reported in Fig. S7A–D), and the evolution of the deformation is shown in Fig. 6E–H. For the elastic

moduli of the first loading phase of bundles, before starting the cyclic phase (Table S7), the values were closer to the ones of the tensile tests, with some differences primarily due to the design of the gripping system. Following this, the bundles became progressively stiffer in the subsequent loading phase due to the increasing compacting of the internal nanofibers. This behavior is also typical of the tendon tissue during the first cycles of oligocyclic tests [58]. Examining the elastic moduli during the initial two loading phases of the bi-material bundles validates the effectiveness of reducing the stress concentration and the strain hardening due to the NY side with the RBCJ. Specifically, the RBCJ shows an initial apparent elastic modulus of $E_A = 49 \pm 7$ MPa. In the second loading phase, the modulus increases to $E_A = 81 \pm 10$ MPa, denoting a 65.3 % increment in modulus.

In contrast, the RBFJ shows an apparent modulus of $E_A = 51 \pm 19$ MPa during the first loading phase. In the second loading phase, it reaches $E_A = 102 \pm 37$ MPa, resulting in a significant increment of 100 % of the elastic modulus. Looking at the typical shape of the initial loading phase of the stress–strain curves of bundles (Fig. 6A–D and Fig. S7), it was notable that all the bundles showed an initial toe region typical of the target biological tissues [5,52], and the trend was maintained during the whole cyclic tests. Furthermore, the shape of the toe region of RBFJ (Fig. 6C and Fig. S7C) mimics the ones of RBPU (Fig. 6B and Fig. S7B), while RBCJ (Fig. 6D and Fig. S7D) recalls the shape of RBNY (Fig. 6Aand Fig. S7A). The net mechanical properties of bundles generally resulted in 2–3 times higher values than the apparent ones.

The evolution of the deformation during the 10 loading phases of each first cycle of each package was best fitted with the exponential decay equation (Fig. 6E–H and Table S8). The coefficients a and b were evaluated by best fitting and summarized together with the coefficient of determination R^2 in Table 1.

The parameter (a) indicates the exponential initial quantity and, therefore, the deformation after the first loading phase. The RBNY showed the lowest initial deformation $\Delta\varepsilon_{\text{RBNY}} = 2.8 \pm 0.1$ %, while the RBPU showed the highest initial deformation $\Delta\varepsilon_{\text{RBPU}} = 7.6 \pm 0.7$ % (Table S8). The bi-material bundles exhibited, instead, intermediate initial deformations compared to the ones of RBNY and RBPU. Notably, RBCJ had a lower initial deformation $\Delta\varepsilon_{\text{RBCJ}} = 4.8 \pm 0.1$ % compared to
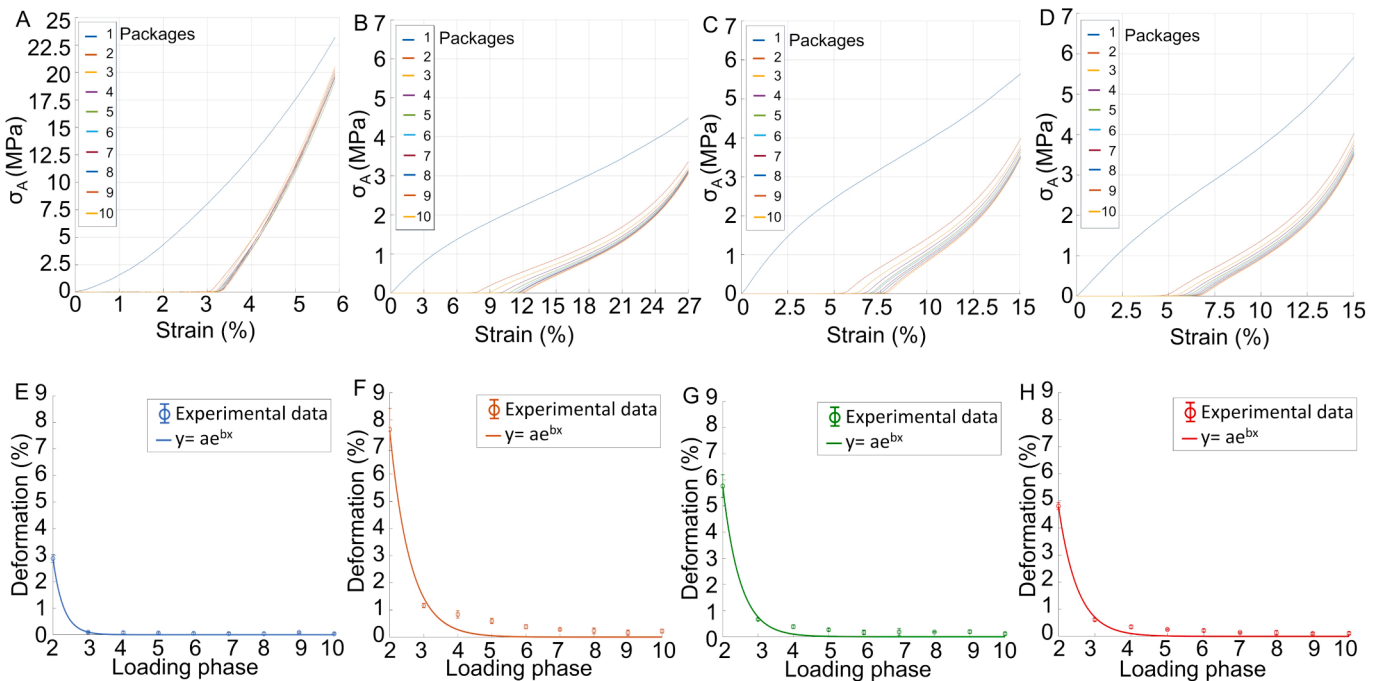

Fig. 6. Typical loading phase of apparent stress–strain curves for each package of the cyclic tests: A) RBNY; B) RBPU; C) RBFJ; D) RBCJ. Evolution of the initial deformation of bundles (mean ± SD between all the specimens for each sample category): E) RBNY; F) RBPU; G) RBFJ; H) RBCJ.

Table 1

Fitting parameters of the deformation curve of bundles in the n + 1 loading phases of the cyclic tests.

	a	b	R^2
RBNY	2.8	−2.91	0.996
RBPU	7.6	−1.66	0.977
RBFJ	5.8	−2.025	0.989
RBCJ	4.8	−1.903	0.987

the RBFJ $\Delta\varepsilon_{RBFJ} = 5.8 \pm 0.4$ %. In the last package, RBFJ ($\Delta\varepsilon_{RBFJ} = 0.11 \pm 0.06$ %) and RBCJ ($\Delta\varepsilon_{RBCJ} = 0.11 \pm 0.05$ %) significantly reduced their deformations, showing intermediate values compared to the RBPU ($\Delta\varepsilon_{RBPU} = 0.22 \pm 0.1$ %) and the RBNY, which maintained the lowest values of deformation ($\Delta\varepsilon_{RBNY} = 0.03 \pm 0.03$ %). The parameter (b) instead, indicates the deformation's decay rate. RBPU had the lowest rate, while RBNY was the fastest one. This fact means that RBPU progressively deformed as the cycles increased, while RBNY deformed entirely after the first package, and then the deformation remained stable.

The bi-material bundles showed an intermediate value of the parameter (b) compared to the two pure materials. Specifically, RBCJ had a lower decay rate, confirming the conical junction's ability to reduce the deformations of the bi-material bundles as the cycles increased (Table 1).

Finally, it is fundamental to mention that all the bundles successfully concluded all the cyclic tests without breaking, proving themselves promising for load-bearing applications.

3.5. Comments for material design

A bi-material bundle's design must consider the mechanical behavior of the constituent materials and the joint area between them. This study focused on two constituent materials, NY and PU, linked by two types of joints: flat and conical. The flat junction is relatively simple to realize by electrospinning but has an abrupt geometric transition from one material to the other, causing a stress concentration. The conical junction, more complex to manufacture, is inspired by MTJ, and its geometry allows for a gradual transfer of stresses. The static and cyclic characterizations of the two constituent nanofibrous materials and the two junctions provided fundamental results applicable to the design of bi-material bundles.

RBNY showed a stiffness about 5 times higher than RBPU, while the failure strain of RBPU was about 10 times higher than that of RBNY, with a related net failure stress about 6 times lower than that of RBNY.

The bi-material bundles were designed so that the mass percentage of NY nanofibers was about 40 % of the total in both RBFJ and RBCJ. The bi-material bundles showed an intermediate static tensile mechanical behavior between the two constituents. In particular, for both RBFJ and RBCJ, it was observed that the failure strain was about 4 times higher than that of RBNY and about 3 times lower than that of RBPU. Moreover, the failure strain of bi-material bundles was not affected by the type of joint and was around 60 % lower compared to RBPU while reaching the same failure stress values. On the other hand, the stiffness of the bi-material bundles was significantly influenced by the type of junction: RBCJ has a net elastic modulus approximately 40 % higher than RBFJ.

Cyclic tests were conducted with imposed displacement, a typical working condition in soft robotics. Tests on RBNY revealed, for the first time in the literature, an alternating stiffening and softening phenomenon, in a range of about 5 %, when cycled. In soft robotics applications, this phenomenon is critical since stiffening, when alternated with softening, can induce an unstable control. This issue is completely overcome thanks to bi-material bundles. From the stress variation point of view, the PU in the bi-material bundles makes it possible to compensate the stiffening and softening effects occurring in NY. In particular, RBCJ exhibits an initial softening, with a loss of 9 % in stiffness, that lasts up to

about 40,000 cycles (see Fig. 5 and Table S5). In the case of RBFJ, the training ends after about 30,000 cycles with a stiffness reduction of about 6 %. After the initial training, RBCJ were observed to have 30 % more stiffness than RBFJ. In both cases, the material stiffness is maintained up to at least 100,000 cycles after training. Therefore, focusing on soft robotics, a conical junction should be preferred if a transmission with high stiffness and precision is desired (i.e. grasping tasks), as in the physiological case of MTJs of tendons and muscles dedicated to fast and precise movements (such as the ones of hands and fingers). Conversely, if a transmission with greater compliance is desired, a flat junction between the two materials should be more suitable. Moreover, further stiffness tuning may be achieved by adjusting the PU and NY weight percentages in the junctions, which are fixed in this work, to further adapt the stiffness according to the required application [59].

4. Conclusions

In this work, aligned-to-aligned mats of different polymers have been matched and scaled up to reach a more complex hierarchical structure, mimicking the muscle–tendon fascicle level and its junction. Electrospun bundles of aligned nanofibers of PU (muscle fascicle side) and NY (tendon fascicle side) were produced. A versatile and easy method to produce electrospun bi-material bundles with separate regions of aligned nanofibers of PU and NY connected with myotendinous-inspired junctions (i.e. flat and conical configurations), was successfully developed. The morphological investigation of nanofibers and bundles, through SEM and microCT, revealed that PU and NY nanofibers were axially aligned and with diameters, for nanofibers and bundles, in the same range as the natural tissue counterparts. The investigation also showed that the conical junctions closely mimic the natural myotendinous junction structure better than the flat one. The tensile mechanical characterization revealed that both the bi-material junctions reached stress at failure comparable to the PU bundles, whereas the strain at failure showed an intermediate value between the pure NY and PU bundles. Specifically, the conical one seemed better at replicating the mechanical behavior of the natural myotendinous junction, reporting stiffness and elastic modulus values higher than the flat one and the PU. Moreover, cyclic tensile tests, carried out by cyclizing within the elastic range of bundles, demonstrated that all the bundles were able to withstand the test without breaking. NY bundles showed an unexpected hardening during cycles, while the other sample categories showed an initial slow decay of mechanical properties, followed by a rapid stabilization maintained for the entire test. Specifically, this behavior confirmed the junctions' ability to dampen their NY side's hardening over time. The promising results obtained in this study pave the way for further development of a new class of biomimetic electrospun junctions with potential applications in soft robotics and interfacial tissue engineering.

Declaration of competing interest

The authors declare that they have no known competing financial interests or personal relationships that could have appeared to influence the work reported in this paper.

Data availability

Data will be made available on request.

Acknowledgments

Appendix A. Supplementary data

Supplementary data to this article can be found online at https://doi.org/10.1016/j.matdes.2024.113015.

References

[1] O. Yasa, Y. Toshimitsu, M.Y. Michelis, L.S. Jones, M. Filippi, T. Buchner, R. K. Katzschmann, An Overview of Soft Robotics, Annu. Rev. Control. Robot. Auton. Syst. 6 (2023) 1–29, https://doi.org/10.1146/annurev-control-062322-100607.

[2] K. Asaka, H. Okuzaki, Soft Actuators: Materials, Modeling, Applications, and Future Perspectives: Second Edition, Second, Asaka and Okuzaki, 2019. doi:10.1007/978-981-13-6850-9.

[3] C. Gotti, A. Sensini, A. Zucchelli, R. Carloni, M.L. Focarete, Hierarchical fibrous structures for muscle-inspired soft-actuators: A review, Appl. Mater. Today. 20 (2020) 100772, https://doi.org/10.1016/j.apmt.2020.100772.

[4] C. Laschi, M. Cianchetti, Soft robotics: New perspectives for robot bodyware and control, Front. Bioeng, Biotechnol. 2 (2014) 1–5, https://doi.org/10.3389/fbioe.2014.00003.

[5] W. Murphy, J. Black, G. Hastings, Handbook of Biomaterial Properties, Second, Springer (2016), https://doi.org/10.1007/978-1-4939-3305-1.

[6] D.E. Rassier, Muscle Biophysics: From Molecules to Cells., 1st ed., Springer New York, NY, 2010. doi:https://doi.org/10.1007/978-1-4419-6366-6.

[7] W.R. Frontera, J. Ochala, Skeletal Muscle: A Brief Review of Structure and Function, Behav. Genet. 45 (2015) 183–195, https://doi.org/10.1007/s00223-014-9915-y.

[8] P. Kannus, Structure of the tendon connective tissue, Scand. J. Med. Sci. Sport. 10 (2000) 312–320, https://doi.org/10.1034/j.1600-0838.2000.010006312.x.

[9] N.C. Apostolopoulos, Stretch Intensity and the Inflammatory Response: A Paradigm Shift, 1st ed., Springer International Publishing, Cham, 2018. doi:https://doi.org/10.1007/978-3-319-96800-1.

[10] E. Bayrak, P.Y. Huri, Engineering musculoskeletal tissue interfaces, Front. Mater. 5 (2018) 1–8, https://doi.org/10.3389/fmats.2018.00024.

[11] S.P. Nukavarapu, J.W. Freeman, C.T. Laurencin, Regenerative Engineering of Musculoskeletal Tissues and Interfaces, 1st ed., Woodhead Publishing, 2015. doi:https://doi.org/10.1016/C2014-0-02826-2.

[12] W. Hwang, N.G. Kelly, A.M. Boriek, Passive mechanics of muscle tendinous junction of canine diaphragm, J. Appl. Physiol. 98 (2005) 1328–1333, https://doi.org/10.1152/japplphysiol.00816.2004.

[13] J.M. Grasman, M.J. Zayas, R.L. Page, G.D. Pins, Biomimetic scaffolds for regeneration of volumetric muscle loss in skeletal muscle injuries, Acta Biomater. 25 (2015) 2–15, https://doi.org/10.1016/j.actbio.2015.07.038.

[14] J. Liu, D. Saul, K.O. Böker, J. Ernst, W. Lehman, A.F. Schilling, Current Methods for Skeletal Muscle Tissue Repair and Regeneration, Biomed Res. Int. 2018 (2018) 1–11, https://doi.org/10.1155/2018/1984879.

[15] K.H. Nakayama, M. Shayan, N.F. Huang, Engineering Biomimetic Materials for Skeletal Muscle Repair and Regeneration, Adv. Healthc. Mater. 8 (2019) 1–14, https://doi.org/10.1002/adhm.201801168.

[16] S.Y. Severt, S.L. Maxwell, J.S. Bontrager, J.M. Leger, A.R. Murphy, Mimicking muscle fiber structure and function through electromechanical actuation of electrospun silk fiber bundles, J. Mater. Chem. B. 5 (2017) 8105–8114, https://doi.org/10.1039/c7tb01904a.

[17] F. Alshomer, C. Chaves, D.M. Kalaskar, Advances in tendon and ligament tissue engineering : materials perspective, J. Mater. 2018 (2018) 1–18, https://doi.org/10.1155/2018/9868151.

[18] M.E. Gomes, R.L. Reis, M.T. Rodrigues, Tendon Regeneration: Understanding Tissue Physiology and Development to Engineer Functional Substitutes, 2015.

[19] G. Yang, B.B. Rothrauff, R.S. Tuan, Tendon and ligament regeneration and repair: Clinical relevance and developmental paradigm, Birth Defects Res, Part C - Embryo Today Rev. 99 (2013) 203–222, https://doi.org/10.1002/bdrc.21041.

[20] I.L. Sander, N. Dvorak, J.A. Stebbins, A.J. Carr, P.A. Mouthuy, Advanced robotics to address the translational gap in tendon engineering, Cyborg Bionic Syst. 2022 (2022), https://doi.org/10.34133/2022/9842169.

[21] A. Sensini, L. Cristofolini, Biofabrication of electrospun scaffolds for the regeneration of tendons and ligaments, Materials (basel). 11 (2018) 1963, https://doi.org/10.3390/ma11101963.

[22] N. Narayanan, C. Jiang, G. Uzunalli, S.K. Thankappan, C.T. Laurencin, M. Deng, Polymeric electrospinning for musculoskeletal regenerative engineering, Regen. Eng. Transl. Med. 2 (2016) 69–84, https://doi.org/10.1007/s40883-016-0013-8.

[23] L.A. Bosworth, S. Downes, Electrospinning for tissue regeneration, first, woodhead publishing, Cambridge (2011), https://doi.org/10.1016/B978-1-84569-741-9.50001-X.

[24] C. Akduman, E.P.A. Kumbasar, Electrospun Polyurethane Nanofibers, in: F. Yilmaz (Ed.), Asp. Polyurethanes, 1st ed., IntechOpen, 2017: pp. 17–59. doi:10.5772/intechopen.69937.

[25] C. Gotti, A. Sensini, G. Fornaia, C. Gualandi, A. Zucchelli, M.L. Focarete, Biomimetic hierarchically arranged nanofibrous structures resembling the architecture and the passive mechanical properties of skeletal muscles : a step forward toward artificial muscle, Front. Bioeng. Biotechnol. 8 (2020) 767, https://doi.org/10.3389/fbioe.2020.00767.

[26] S.V. Ebadi, H. Fashandi, D. Semnani, B. Rezaei, A. Fakhrali, Electroactive actuator based on polyurethane nanofibers coated with polypyrrole through electrochemical polymerization: A competent method for developing artificial muscles, Smart Mater. Struct. 29 (2020), https://doi.org/10.1088/1361-665X/ab73e5.

[27] S.L. Cooper, J. Guan, Advances in Polyurethane Biomaterials, 1st ed., Elsevier, 2016. doi:10.1016/B978-0-08-100614-6.00017-2.

[28] J.K. Kwon, H.J. Yoo, J.W. Cho, Conducting core-sheath polyurethane-PEDOT nanofibres for conducting polymer actuator, Int. J. Nanotechnol. 10 (2013) 661–670, https://doi.org/10.1504/IJNT.2013.054208.

[29] S.V. Ebadi, D. Semnani, H. Fashandi, B. Rezaei, Highly conductive Faradaic artificial muscle based on nanostructured polypyrrole-bis(trifluoromethylsulfonyl) imide synthesized onto electrospun polyurethane nanofibers, Sensors Actuators, B Chem. 297 (2019), https://doi.org/10.1016/j.snb.2019.126736.

[30] G. Khang, Handbook of Intelligent Scaffolds for Tissue Engineering and Regenerative Medicine, 2nd ed., Pan Stanford Publishing, Singapore, 2017.

[31] A. Sensini, C. Gotti, J. Belcari, A. Zucchelli, M.L. Focarete, C. Gualandi, I. Todaro, A.P. Kao, G. Tozzi, L. Cristofolini, Morphologically bioinspired hierarchical nylon 6,6 electrospun assembly recreating the structure and performance of tendons and ligaments, Med. Eng. Phys. 71 (2019), https://doi.org/10.1016/j.medengphy.2019.06.019.

[32] A. Sensini, M.H. Santare, E. Eichenlaub, E. Bloom, C. Gotti, A. Zucchelli, L. Cristofolini, Tuning the structure of nylon 6,6 electrospun bundles to mimic the mechanical performance of tendon fascicles, Front. Bioeng Biotechnol. 9 (2021) 1–12, https://doi.org/10.3389/fbioe.2021.626433.

[33] J.K. Kim, S. Tadokoro, Electroactive polymers for robotic applications, Springer (2007), https://doi.org/10.1007/978-1-84628-372-7.

[34] H. Wang, R. Zhang, W. Chen, X. Wang, R. Pfeifer, A cable-driven soft robot surgical system for cardiothoracic endoscopic surgery: preclinical tests in animals, Surg. Endosc. 31 (2017) 3152–3158, https://doi.org/10.1007/s00464-016-5340-9.

[35] R. Wang, X. Zhang, B. Zhu, H. Zhang, B. Chen, H. Wang, Topology optimization of a cable-driven soft robotic gripper, Struct. Multidiscip. Optim. 62 (2020) 2749–2763, https://doi.org/10.1007/s00158-020-02619-y.

[36] U. Jeong, K. Kim, S.H. Kim, H. Choi, B.D. Youn, K.J. Cho, Reliability analysis of a tendon-driven actuation for soft robots, Int. J. Rob. Res. 40 (2021) 494–511, https://doi.org/10.1177/0278364920907151.

[37] M.R. Ladd, S.J. Lee, J.D. Stitzel, A. Atala, J.J. Yoo, Co-electrospun dual scaffolding system with potential for muscle-tendon junction tissue engineering, Biomaterials. 32 (2011) 1549–1559, https://doi.org/10.1016/j.biomaterials.2010.10.038.

[38] A. Sensini, G. Massafra, C. Gotti, A. Zucchelli, L. Cristofolini, Tissue engineering for the insertions of tendons and ligaments: an overview of electrospun biomaterials and structures, Front. Bioeng Biotechnol. 9 (2021) 1–23, https://doi.org/10.3389/fbioe.2021.645544.

[39] R.K. Tindell, L.P. Busselle, J.L. Holloway, Magnetic fields enable precise spatial control over electrospun fiber alignment for fabricating complex gradient materials, J. Biomed. Mater. Res. - Part A. 111 (2023) 778–789, https://doi.org/10.1002/jbm.a.37492.

[40] C.N. Joyce Chen, L.D.V. Thompson, L.A. Snow, Muscle Structure and Function, in: Jeffrey D. Placzek, David A. Boyce (Eds.), Orthop. Phys. Ther. Secrets Third Ed., 3rd ed., Elsevier Inc., 2017: pp. 1–9. doi:10.1016/B978-0-323-28683-1.00001-1.

[41] A. Sensini, C. Gotti, J. Belcari, A. Zucchelli, M.L. Focarete, C. Gualandi, I. Todaro, A.P. Kao, G. Tozzi, L. Cristofolini, Morphologically bioinspired hierarchical Nylon 6.6 electrospun assembly recreating the structure and performance of tendons and ligaments, Med. Eng. Phys. 71 (2019) 79–90, https://doi.org/10.1016/j.medengphy.2019.06.019.

[42] Z. Liu, Scale space approach to directional analysis of images, Appl. Opt. 30 (1991) 1369–1373, https://doi.org/10.1364/AO.30.001369.

[43] J. Schindelin, I. Arganda-Carreras, E. Frise, V. Kaynig, M. Longair, T. Pietzsch, S. Preibisch, C. Rueden, S. Saalfeld, B. Schmid, J.-Y. Tinevez, D.J. White, V. Hartenstein, K. Eliceiri, P. Tomancak, A. Cardona, Fiji: an open-source platform

for biological-image analysis, Nat. Methods. 9 (2012) 676–682, https://doi.org/10.1038/nmeth.2019.

[44] A. Sensini, L. Cristofolini, M.L. Focarete, J. Belcari, A. Zucchelli, A. Kao, G. Tozzi, High-resolution x-ray tomographic morphological characterisation of electrospun nanofibrous bundles for tendon and ligament regeneration and replacement, J. Microsc. 272 (2018) 196–206, https://doi.org/10.1111/jmi.12720.

[45] A.R. Gillies, R.L. Lieber, Structure and function of the skeletal muscle extracellular matrix, Muscle and Nerve. 44 (2011) 318–331, https://doi.org/10.1002/mus.22094.

[46] S. Mondal, Influence of solvents properties on morphology of electrospun polyurethane nanofiber mats, Polym. Adv. Technol. 25 (2014) 179–183, https://doi.org/10.1002/pat.3220.

[47] C.A. Bashur, R.D. Shaffer, L.A. Dahlgren, S.A. Guelcher, A.S. Goldstein, Effect of fiber diameter and alignment of electrospun polyurethane meshes on mesenchymal progenitor cells, Tissue Eng. Part A 15 (2009) 2435–2445, https://doi.org/10.1089/ten.tea.2008.0295.

[48] P.C. Caracciolo, V. Thomas, Y.K. Vohra, F. Buffa, G.A. Abraham, Electrospinning of novel biodegradable poly(ester urethane)s and poly(ester urethane urea)s for soft tissue-engineering applications, J. Mater. Sci. Mater. Med. 20 (2009) 2129–2137, https://doi.org/10.1007/s10856-009-3768-3.

[49] J. Kastelic, A. Galeski, E. Baer, The multicomposite structure of tendon, Connect. Tissue Res. 6 (1978) 11–23, https://doi.org/10.3109/03008207809152283.

[50] P. Kannus, M. Paavola, L. Józsa, Aging and degeneration of tendons, in: N. Maffulli, P. Renström, L. W.B. (Eds.), Tendon Inj., Springer, London, 2005: pp. 25–31. doi:10.1007/1-84628-050-8_4.

[51] P. Hanson, P. Aagaard, S.P. Magnusson, Biomechanical properties of isolated fascicles of the Iliopsoas and Achilles tendons in African American and Caucasian men, Ann. Anat. 194 (2012) 457–460, https://doi.org/10.1016/j.aanat.2012.03.007.

[52] C. Zhao, S. Wang, G. Wang, M. Su, L. Song, J. Chen, S. Fan, X. Lin, Preparation of decellularized biphasic hierarchical myotendinous junction extracellular matrix for muscle regeneration, Acta Biomater. 68 (2018) 15–28, https://doi.org/10.1016/j.actbio.2017.12.035.

[53] R.L. Lieber, B.I. Binder-Markey, Biochemical and structural basis of the passive mechanical properties of whole skeletal muscle, J. Physiol. 599 (2021) 3809–3823, https://doi.org/10.1113/JP280867.

[54] V. Racic, A. Pavic, J.M.W. Brownjohn, Experimental identification and analytical modelling of human walking forces: Literature review, J. Sound Vib. 326 (2009) 1–49, https://doi.org/10.1016/j.jsv.2009.04.020.

[55] W.L. Phillips, W.O. Statton, Stress-relaxation hardening of nylon 66 filaments, J. Mater. Sci. 5 (1970) 1021–1026, https://doi.org/10.1007/BF02403272.

[56] M. Gazzano, C. Gualandi, A. Zucchelli, T. Sui, A.M. Korsunsky, C. Reinhard, M. L. Focarete, Structure-morphology correlation in electrospun fibers of semicrystalline polymers by simultaneous synchrotron SAXS-WAXD, Polymer (guildf). 63 (2015) 154–163, https://doi.org/10.1016/j.polymer.2015.03.002.

[57] C.D. Kuthe, R.V. Uddanwadiker, Investigation of effect of fiber orientation on mechanical behavior of skeletal muscle, J. Appl. Biomater. Funct. Mater. 14 (2016) e154–e162, https://doi.org/10.5301/jabfm.5000275.

[58] C.R. Firminger, W.B. Edwards, Effects of cyclic loading on the mechanical properties and failure of human patellar tendon, J. Biomech. 120 (2021) 110345, https://doi.org/10.1016/j.jbiomech.2021.110345.

[59] S. Wolf, G. Grioli, O. Eiberger, W. Friedl, M. Grebenstein, H. Hoppner, E. Burdet, D. G. Caldwell, R. Carloni, M.G. Catalano, D. Lefeber, S. Stramigioli, N. Tsagarakis, M. Van Damme, R. Van Ham, B. Vanderborght, L.C. Visser, A. Bicchi, A. Albu-Schaffer, Variable stiffness actuators: review on design and components, IEEE/ASME Trans. Mechatronics. 21 (2016) 2418–2430, https://doi.org/10.1109/TMECH.2015.2501019.